Characterizing the Geometry of Phaeodarian Colonial Spheres

Kate Beittenmiller, Carnegie Mellon University

Mentor: Steve Haddock

Summer 2015

Keywords: Phaeodaria, geodesic sphere or dome, biogenic silica, radiolaria

1. ABSTRACT

A geodesic sphere model was investigated to describe the geometry of phaeodarian colonial spheres. Geodesics of different base geometry and frequency were compared to the overall phaeodarian geometry to identify an icosahedron or dodecahedron base as most suitable. Scanning electron microscopy, optical microscopy, and ImageJ analysis were used to characterize specimens of 3 species of phaeodarian, and this data was used to fit each species with a model. Additionally, phalloidin staining and genetic analysis were used to investigate the silica deposition mechanism.

2. INTRODUCTION

Phaeodaria are deep-sea protozoa, found anywhere from 100 to 3000 meters depth, that feed on detritus falling from the ocean's surface, also known as marine snow. They are now known to be a class of the phylum Cercozoa, but they were historically grouped within Radiozoa. Due to this historical classification, they are sometimes referred to as radiolarians and grouped with the polycistine radiolarians, which do belong in Radiozoa.

Several species of phaeodaria form colonial spheres connecting several silica capsules that surround individual organisms. The spheres are made of an intricate silica network and are largely unstudied because they are too fragile to be preserved in sediment. The majority of specimens have exactly 8 capsules per sphere, though some

have 16 or 32 capsules. Figure 1 shows *T. globosa*, one of the species examined in this paper. The particles visible on the sphere are marine snow.

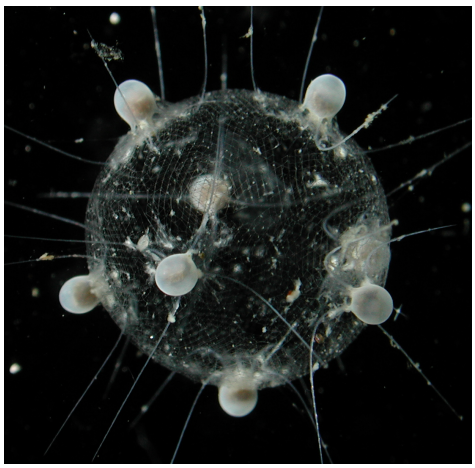

Figure 1. An image of *T. globosa* is shown. The 8 capsules are visible, and a vague lattice pattern can be seen (photo credit to Steve Haddock).

Many organisms in the ocean utilize biomineralization processes to build supporting or protective structures, most commonly using silica and calcium carbonate. Both are used to produce ordered structures, but calcium carbonate is normally present in crystalline form, while silica is most often amorphous. Sponges, diatoms, and radiolarians (polycystine and phaeodarian) are three major types of organisms that produce silica structures. Sponges most commonly produce silica spicules, which are long cylindrical structures ranging from microns to meters in length, formed around an axial filament. Specialized silica deposition proteins, also called silicateins, make up 95 % of this filament and are thought to be the primary mechanism by which silica structures are formed in sponges. Diatoms, on the other hand, have vesicles called silica deposition vehicles (SDVs), whose acidic conditions promote gelation of silica from ambient silicic acid into nanoparticles. These nanoparticles are then deposited and fuse together to form a frustule. The surface of the frustule is covered in evenly spaced and equally sized pores. Depending on species and specimen, the pore diameter ranges from nano- to micrometer length[1]. While diatoms and sponges have received considerable attention, radiolarians are relatively unstudied, and their silica deposition mechanism is unknown. It is possible that they utilize the same mechanism as either sponges or diatoms, but they may have a mechanism of their own.

Silica is one of the most common materials on the planet, and it has many uses. Silica is manufactured as a precursor to glass products such as windows, tableware, and optical fibers. It can also be refined into elemental silicon for use in computers and other electronics. Ordered nanostructures like that of the diatoms have specialized biomedical applications such as drug delivery and use as biosensors. Currently, widely used silica manufacturing processes require highly acidic conditions, high temperatures, or both. Understanding how marine organisms deposit silica in more moderate temperatures and

pH levels could allow for improvement of the manufacturing process, lowered cost of production, and greater control over mesoscale structural properties[2].

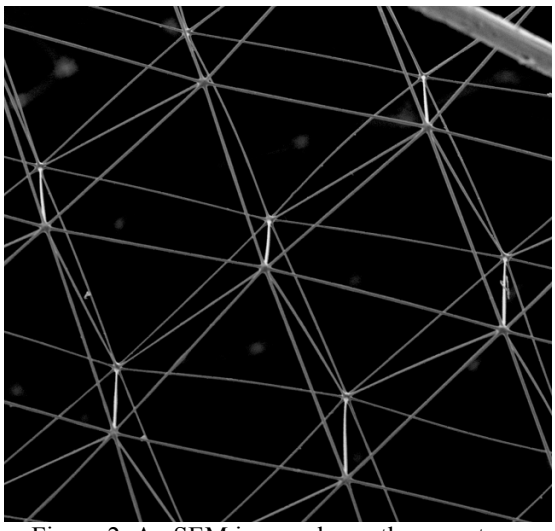

Figure 2. An SEM image shows the repeat unit of the phaeodarian silica lattice: a hexagonal prism with additional cross-supports on two of the three hexagonal axes (photo credit to Steve Haddock).

Phaeodarian colonial spheres exhibit complex and regular geometry. Characterization and modeling of such geometry can provide insight into how the structures are formed. The structure of phaeodarian colonial spheres is best observed using a scanning electron microscope (SEM). The spheres are composed of a double layer of many near-equilateral triangles arranged in a hexagonal lattice. The two layers are connected with vertical rods at each vertex and diagonal supports on two of the three sides of each triangle. Figure 2 shows the observed repeat unit: a hexagonal prism as previously described.

A geodesic sphere, a well-studied geometric structure, is also composed of all equilateral triangles and has emerged as a potential model for the phaeodarian spheres. Geodesic domes were popularized by Buckminster Fuller as a means of building large domes without internal column supports, and they have the additional advantage of being simple to assemble because each face is identical. Because equilateral triangles distribute stress evenly along their three sides, geodesic spheres are able to distribute stress evenly throughout their entire structure. This makes them exceptionally strong for the amount of material they require. Thus, they would be an efficient biological structure to expend minimal building material and energy for maximal strength[3].

Geodesic spheres are described by their base polyhedron and frequency, k. Frequency describes the number of subdivisions of each face of the base polyhedron. At k=1, each face is divided into triangles whose vertices are then projected onto the sphere circumscribed about the polyhedron. At k=2, each of these resultant faces is divided into four more triangles whose vertices are projected, and so on. Figure 3 shows an illustration

of frequency. Because the faces are divided and not otherwise changed, the vertices of the base polyhedron are always preserved in the resultant sphere.

Species of phaeodarian can be distinguished by the number and shape of spines coming off of each capsule. Two species of interest in this report are *Tuscaridium cygneum* and *Tuscaretta globosa*. *T. cygneum* has four spines extending from the base of the capsule and one outward from the top. The spines at the base, called oral spines, follow the surface of the sphere in plane with the surface of the sphere. *T. globosa* has four oral spines, and they extend downward from the base of the capsule to curve inside and then back out through the sphere. A third phaeodarian species of interest is *Aulosphaera*. It does not form a colonial sphere with other organisms, but instead builds one sphere for each organism and exists as colonial clusters of spheres. *Aulosphaera* was chosen because its spheres retain the geodesic shape, but they have only one layer, simplifying the hexagonal repeat unit, and the faces of the sphere are larger relative to the sphere diameter, simplifying the overall shape.

3. MATERIALS AND METHODS

Images of *T. cygneum* and *T. globosa* were taken using the scanning electron microscope (SEM) at Moss Landing Marine Labs, and images of *Aulosphaera* were taken using an optical microscope and digital camera. Image and data analysis was done using ImageJ and R. Models were generated using R's mvmesh package and Wolfram Mathematica's PolyhedonData package.

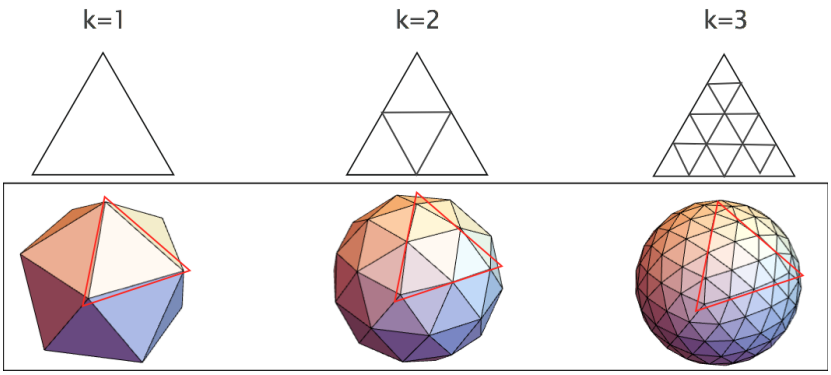

Figure 3. Frequencies 1 to 3 for an icosahedron-based geodesic sphere are shown, highlighting the subdivision of faces as the defining factor of increased frequency.

3.1 MEASURING SPECIMENS

To analyze the structure of phaeodarian spheres, measurements were taken from SEM images using ImageJ image analysis software. All of the images analyzed were taken using the SEM at Moss Landing Marine Labs. For three different species, *T. globosa*, *T. cygneum*, and *Aulosphaera*, measurements were taken of sphere diameter and triangle side lengths. Due to limited SEM access and varying sample availability, the number of measurements varies for the different species, but the measurements do provide some insight as to the side length distributions. Because the surface of the sphere is curved, there is potential distortion of the measurements as the sphere curves away from the image plane. To minimize this, only sections of the image in which the sphere surface appears most parallel to the image plane, usually the center of the image, were chosen. Additionally, for the colonial species, *T. globosa* and *T. cygneum*, each triangle is so small in relation to the sphere that distortion was assumed to be negligible. However, distortion may have a greater effect on the *Aulosphaera* measurements because the same number of measurements must span greater curvature.

3.2 FITTING THE MODEL

Geodesic models were generated for octahedral, cubic, icosahedral, and dodecahedral bases from frequencies k = 1 to 8. The octahedral and cubic bases showed increasing distortion of faces at higher frequencies, as shown in Figure 4, thus icosahedra and dodecahedra were identified as the bases of interest for this model.

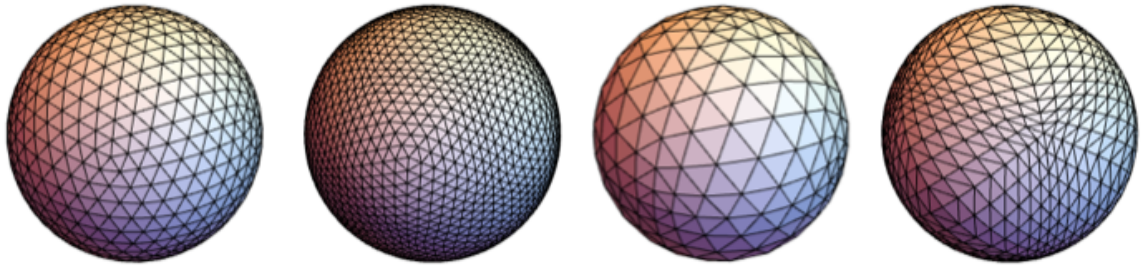

Figure 4. From left to right, icosahedron-, dodecahedron-, octahedron-, and cube-based spheres of frequency k=4 are shown. Distortion is visible on the octahedron- and cube-based spheres, with smaller faces near the original vertices and square symmetry still visible, while the icosahedron- and dodecahedron-based spheres show uniform face size.

The number of faces for icosahedron- and dodecahedron-based spheres from k=1 to 6 were calculated. Then, each species was matched to the model with the nearest

number of faces to its estimated number of faces from measurement. The difference between the calculation and the model was expected to be relatively large because of the irregularity of the specimen spheres compared to the models and because of error and variability in measurement and calculation.

3.3 ADDITIONAL LINES OF INQUIRY

In addition to the geodesic model fit, two additional lines of inquiry were pursued to lesser depth in an attempt to better understand the silica structure and deposition mechanism. These were transcriptome analysis and phalloidin staining.

3.3.1 Genetic Analysis

Because the silica deposition mechanism of sponges has been studied to a greater extent than that of radiolarians, the amino acid sequences of sponge silica deposition proteins, or silicateins, are known for many species. Transcriptome analysis was conducted by searching the NCBI online database for silicatein and cathepsin-L protein sequences, and comparing them to MBARI's own radiolarian transcriptome library using the Geneious software. The MBARI data was first translated from nucleotide sequences into amino acid sequences and then compared to the NCBI sequences. FigTree software was used to create a genetic tree showing the relative similarity of sequences and groups of sequences.

3.3.2 Phalloidin Staining

Phalloidin 488 is a green fluorescent stain that attaches to actin in the cytoskeleton of cells. Because it is possible that contact with the radiolarian cells/cytoplasm is necessary for silica deposition, phalloidin was used to investigate where the cells extended to outside of the capsules. Phalloidin staining was conducted on board the Western Flyer on specimens of *T. globosa, T. campanella, T. luciae,* and *Aulosphaera*. A solution was prepared of 4% formalin and 1% Triton X 100. The phalloidin was reconstituted in 500 μL methanol. For each sample, a solution was prepared consisting of 25 μL phalloidin, 20 mL formalin and Triton solution, and 30 mL seawater. The specimen was immersed in this solution and then incubated in dark

conditions for intervals varying from 1 to 24 hours and observed periodically for fluorescence under the microscope. Additionally, two stained samples were observed under a higher quality microscope back at MBARI.

4. RESULTS

4.1 Geodesic Model Fit

Figure 5 shows histograms of the measured triangle side lengths for the three species. The individual length measurements for each species are given in Appendix A. Table 1 shows the average side length and diameter measured for each species, as well as the number of faces estimated to be on the sphere. The estimation was calculated by dividing the surface area of the sphere by the area of the average triangle. The surface area of the whole sphere can be calculated from the diameter (surface area = $4\pi r^2$), and assuming the triangles are equilateral, the area of one triangle equals $\frac{\sqrt{3}}{4} * (side\ length)^2$. Though the assumption that each triangle is perfectly equilateral and the limited measurements of sphere diameter introduce uncertainty, the estimate still gives an idea of the magnitude of the number of faces for each species. Table 2 shows the number of faces on icosahedron and dodecahedron based geodesic spheres from frequency k=1 to 5. Despite the fact that they can all be modeled using a geodesic sphere, side length and sphere size vary considerably by species, resulting in huge differences in the number of faces expected.

Models were fitted to each species using the number of faces estimated for each species and the number of faces calculated for each frequency of the geodesic model. For example, using *Aulosphaera's* estimated number of faces, 1342, it can be matched to an icosahedron-base geodesic sphere of frequency 3, which has 1280 faces. Figure 6 shows a visual comparison of a microscope image of *Aulosphaera* to the model. *T. globosa* best fits an icosahedron-based sphere of frequency 5, and *T. cygneum* best fits a dodecahedron-based sphere of frequency 6.

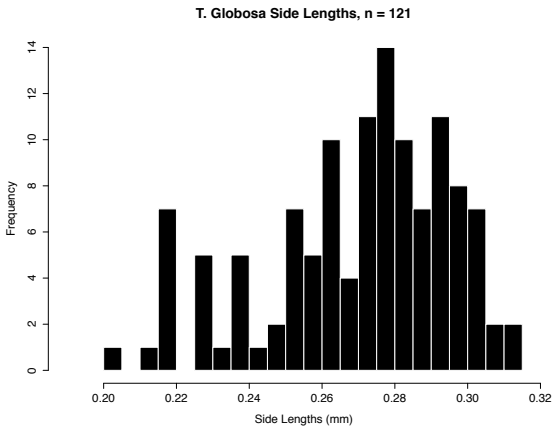

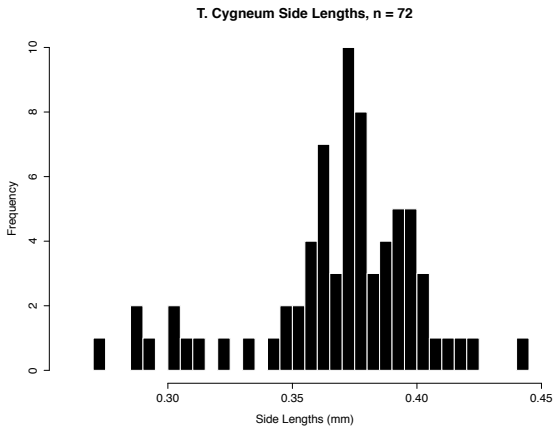

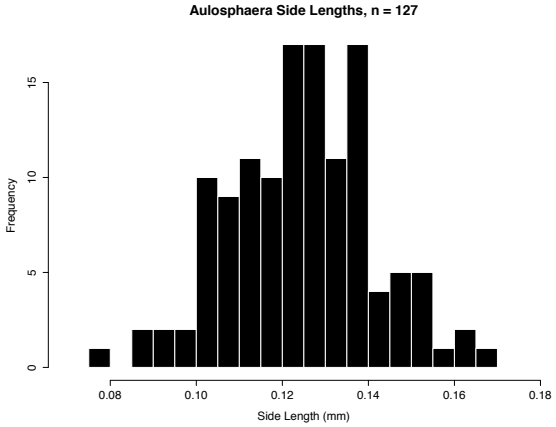

Figure 5. These three histograms show the side length distributions measured for the species *T. globosa* (top left), *T. cygneum* (top right), and *Aulosphaera* (bottom left).

The discrepancy between the specimen's calculated number of faces and the model's number of faces increases dramatically as the size of the sphere increases. This was expected because larger spheres have more areas of irregularity, and more measurements are required to accurately estimate the number of faces on a larger sphere. Additionally, the model's number of faces increases exponentially with frequency as 4^k, leaving larger and larger gaps between one frequency and the next.

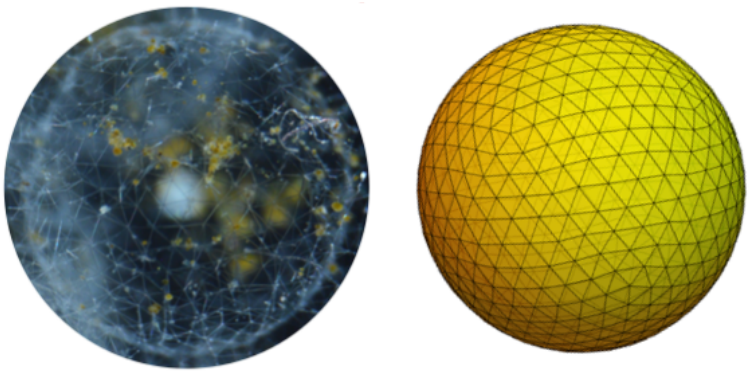

Figure 6. A microscope image of one *Aulosphaera* sphere (left) is shown alongside its icosahedron-based, k=3 geodesic model (right).

Species	Average Side Length	Average Sphere Diameter	Calculated Number of Faces
Aulosphaera	0.125 mm	1.65 mm	1342
T. globosa	0.270 mm	7.97 mm	6495
T. cygneum	0.369 mm	14.41 mm	11386

Table 1. The average side length, average sphere diameter, and calculated number of faces are given for the three species listed. Though the side length increases for each species, the sphere size also increases dramatically, such that the number of faces on a *T. cygneum* sphere is greatest.

Base	k = 1	2	3	4	5	6
Icosahedron	20	80	320	1280	5120	20480
Dodecahedron	12	60	240	960	3840	15360

Table 2. The number of faces for icosahedron and dodecahedron based geodesic spheres from frequency 1 to 6.

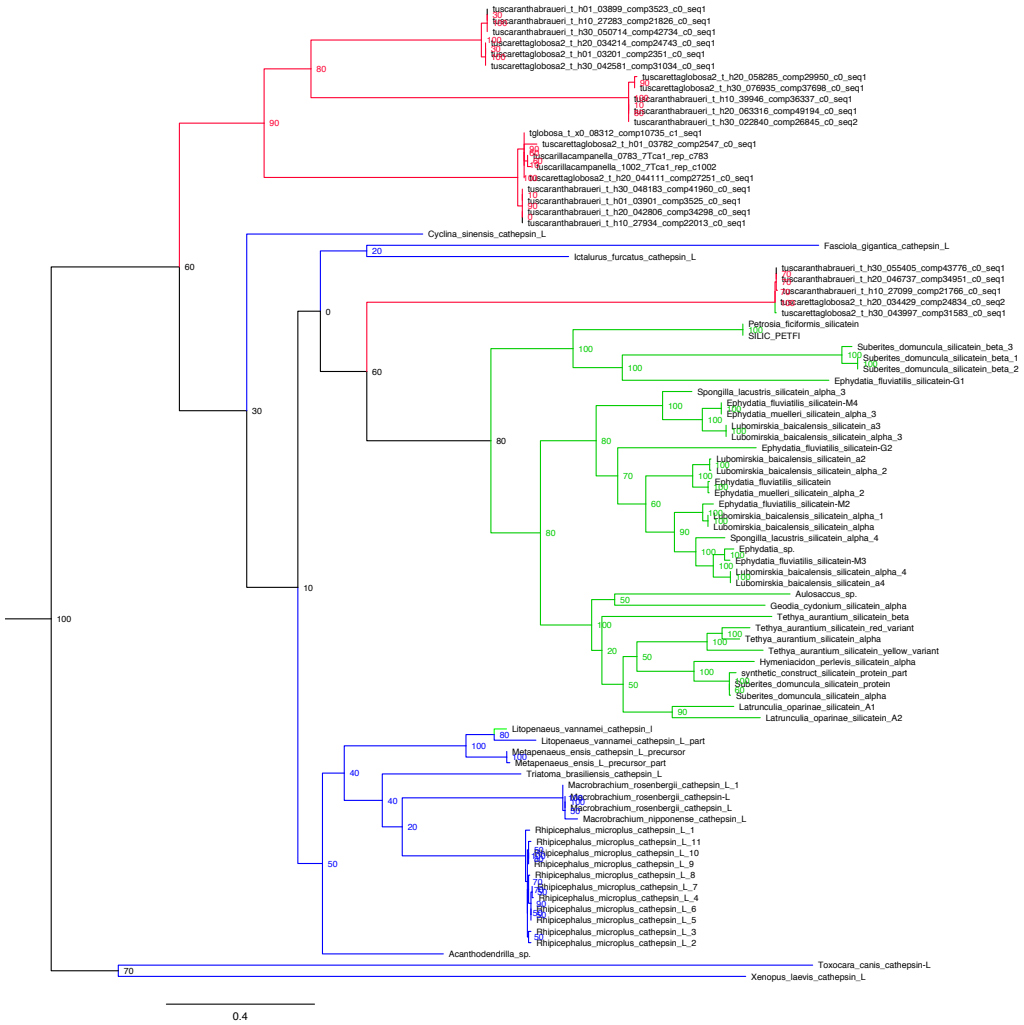

Figure 7. A phylogenetic tree comparing silicatein (green), cathepsin-L (blue), and phaeodarian transcriptome (red) sequences.

4.2 Additional Lines of Inquiry

All phalloidin stained specimens, when observed, showed dim fluorescence inside the capsules. No fluorescence was observed anywhere outside of the capsules for any species, and the fluorescence that was observed was too dim to be visible in microscope images. Upon reexamination at MBARI, the fluorescence was still too dim to capture in images. Figure 7 shows the phylogenetic tree generated from comparison of silicatein, cathepsin-L, and phaeodarian sequences.

5. DISCUSSION

Because phaeodarian spheres so commonly have 8 capsules attached, one might expect the base polyhedron for their sphere to be a cube or octahedron, which have 8 vertices and 8 faces, respectively. However, this do not appear to be correlated, as spheres generated using a cube or octahedron base show high variation in triangle size, many isosceles triangles instead of equilateral, and square traces visible even in high frequency spheres. This is inconsistent with the measured side length distributions, which are unimodal, indicating that faces are roughly equilateral. Figure 4 shows spheres of frequency k = 3 generated using different base polyhedra.

Spheres generated using an icosahedron or dodecahedron base demonstrate much more uniformity in triangle size and length over the surface of the sphere. Because icosahedra and dodecahedra are similar structures (12 faces and 20 vertices versus 20 faces and 12 vertices), their resultant spheres at higher frequencies are nearly identical.

Another important component in the geometry of geodesic spheres is Euler's Law, which states that the number of vertices minus the number of edges plus the number of faces must equal 2 for all convex polyhedra:

$$V - E + F = 2$$

Though the faces of geodesic spheres are triangles, they can be grouped and interpreted as pentagonal and hexagonal faces covering the surface of the sphere. In this case, a rule derivative of Euler's Law becomes important:

$$\sum (6 - n) F_n = 12$$

This formula applies to convex polyhedra with trihedral corners (where three edges meet at one vertex). n is the number of sides on a face and F_n is the number of faces with n sides. The consequence of the (6-n) term is that hexagonal faces essentially do not contribute to the total, so for the geodesic models, polyhedra composed of only hexagonal and pentagonal faces must have exactly 12 pentagonal faces[4]. This applies to the observed sphere because it means that the hexagonal repeat unit identified from SEM cannot be the sole component of the lattice. Figure 8 shows an SEM image of a pentagon observed on the sphere of *T. globosa*. This supports the geodesic sphere as a model for the phaeodarian sphere.

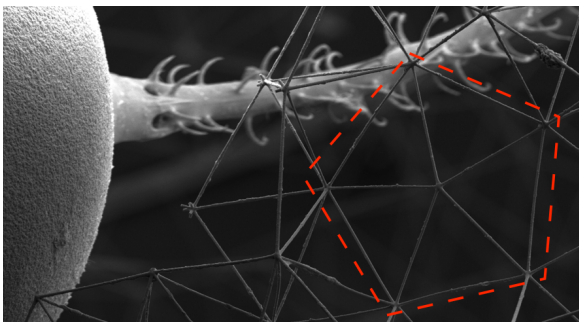

Figure 8. A pentagon was observed in the lattice of a *T. globosa* specimen, as is consistent with Euler's Law of Convex Polyhedra.

Having characterized and modeled the sphere, the question remains as to how they are actually constructed by the organism. Unfortunately, possible growth mechanisms are difficult to rule out due to the fact that silica is an extremely versatile material. O. Roger Anderson discusses silica deposition in radiolarians in his book, *Radiolaria*. He maintains that cytoplasm must be present at the silica surface for deposition to occur and calls this cytoplasm sheath the "cytokalymma", as shown in figure 9-A. He also observes that radiolarians can grow silica rods in a straight line across a gap, as shown in figure 9-B, though no cytokalymma is apparent in that image. To further complicate matters, when Anderson made these observations, there was no distinction made between polycistine radiolarians and phaeodaria, two groups now understood to be genetically distinct, so it is possible that the mechanisms he observed apply to polycistine radiolaria and not phaeodaria[5].

Another mechanism for building complex silica structures is "bio-sintering", as described by Müller, et al (2009). In this method, silica spicules of roughly uniform size are produced by a sponge and then later fuse together by bio-sintering into a network of spicules[6]. Because of the many ways that an organism can manipulate silica in an aqueous environment, even improbable sounding explanations of the phaeodarian sphere must be considered.

One possibility is that the lattice nodes are formed by dispersing silica particles on a spherical interface and then connecting the particles with rods to form the lattice nodes. Bausch et al (2003)

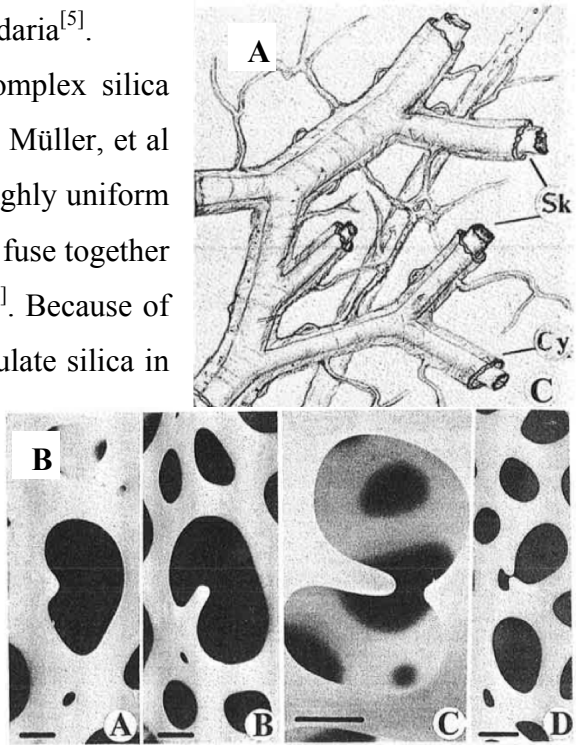

Figure 9. Images from Radiolaria, by O.R. Anderson showing the behavior of silica in radiolaria: (A) the "cytokalymma" (Cy) surrounding the skeleton (Sk), and (B) examples of silica rods joining straight lines across gaps.

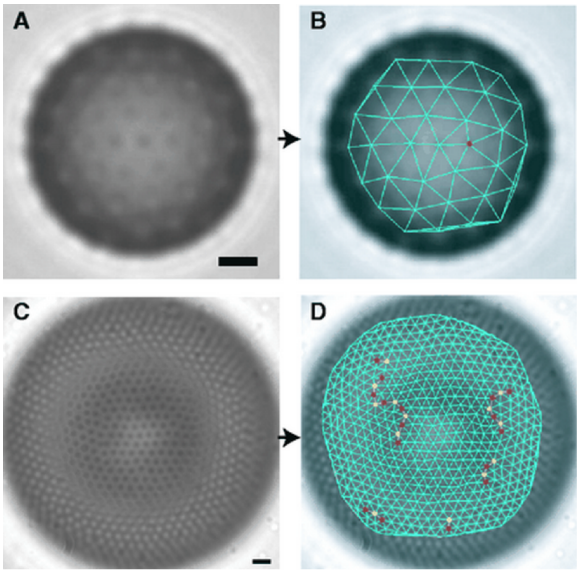

Figure 10. (A) and (C) show particles self-arranged on a spherical interface. (B) and (D) show a lattice drawn between the particles that closely resembles the phaeodarian lattice. On the lattice, red dots mark nodes where only 5 faces meet, and yellow dots mark those where 7 faces meet.

observed that particles of uniform size allowed to move freely in a spherical interface repel and space themselves approximately evenly. When lines were drawn between the particle locations, they formed a two dimensional hexagonal crystal similar to a phaeodarian sphere, as shown in Figure 10[7]. Some species of phaeodaria that do not form silica spheres do form bubbles of cytoplasm that hold multiple organisms together and take on the same general shape of the silica spheres. Thus, it is possible that sphere-forming species could use a similar bubble as a template for the silica lattice.

Because of Euler's Law, the lattice cannot be perfect hexagons, so Bausch et al went on to characterize the defect structures that appeared in their experiment. They found that in systems with few particles relative to sphere size, only the requisite 12 isolated pentagonal defects formed. However, as the size of the system and particle packing on the sphere increased, heptagonal defects appeared, and the pentagonal and heptagonal defects formed "scars", or defect chains, of alternating 5-7 nodes. It appears that the defects form together so that tension around a node with one too few connections is mitigated by compression around a node with one too many. The length of these defect chains increases proportionally to the ratio of sphere radius to mean particle spacing (R/a), and defect chains are expected to appear for all $R/a > 5$[7].

Using measurements from *T. globosa*, which give R/a = 13.8, and the model proposed by Bausch et al, about 5 defects (in addition to one pentagons) are expected in each defect chain. Similarly, for *T. luciae*, about 7 additional defects are expected. No heptagonal defects or defect chains were observed on any of the phaeodarian samples. However, with few expected defects compared to thousands or tens of thousands of faces

on each sphere, this mechanism of particles dispersing on an interface has not been ruled out as a possibility.

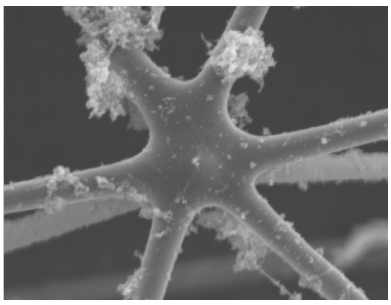

Figure 11. A typical node shows angular asymmetry where pairs of rods meet.

Another possibility for sphere formation is that rods and triangles are produced at one or more point sources and later fuse together to create the lattice. Many nodes are asymmetrical in a way that indicates fusion of two or more prior nodes. For example, Figure 11 shows a node in which every other angle between rods appears to be wider. This asymmetry could be the result of three pre-formed triangle nodes fusing together to form the new node. A second example in Figure 12-A shows an apparently freestanding triangle just above a highly asymmetric node. The end of the freestanding triangle nearest to the node is rounded and does not appear to have broken off of any other node. Figure 12-B shows a close-up of the two nodes. On a larger scale than individual nodes, a lattice with multiple points of origin would have noticeable interfaces where two regions meet. These are analogous to grain boundaries in that they are disordered interfaces where two regions of the same crystal with different crystallographic orientations meet. Figure 13 shows one such boundary. The left half of the image and bottom right of the image show two regular lattices with different orientations. The bottom right lattice is rotated 90° in relation to the left side lattice, such that they cannot merge to form a unified lattice. Instead, a disordered region forms between them, as seen in the center right of the image.

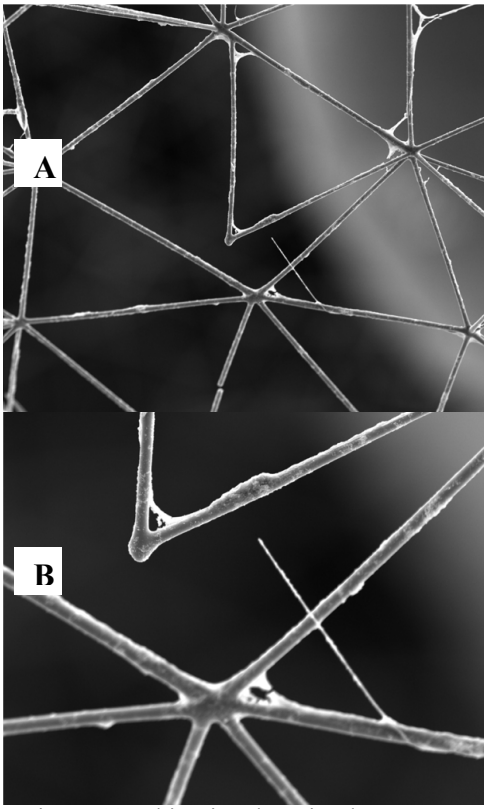

Figure 12. This triangle point does not appear to have broken off of the adjacent node, indicating that individual triangles may be the first level of lattice formation.

A drawback of this theory is that the location of the points of origin is unknown. No correlation was found between the locations of capsules on the sphere and the appearance of

grain boundaries, and regions of irregularity are frequently larger than a small interface and cannot be explained by grain boundaries alone. Additionally, all of the same objections regarding the "cytokalymma" and other theories as to the silica deposition mechanism required for growth and fusion continue to apply in this case.

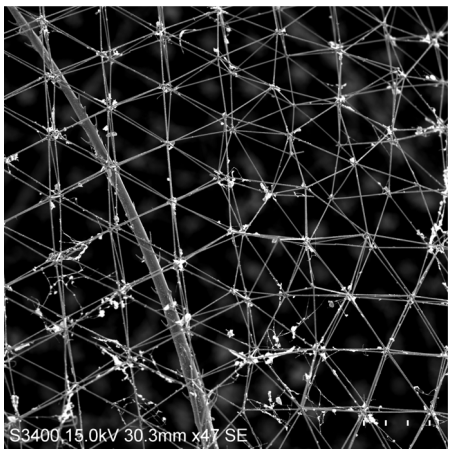

Figure 13. An SEM image shows two regions of regularity (left half and bottom right corner) with an interface of irregularity where the two regions may have grown together.

The phalloidin staining and genetic analysis were inconclusive in eliminating any potential silica deposition mechanisms. The phalloidin staining was completely inconclusive. Despite the fact that fluorescence was observed only in the capsules, it is already known that radiolaria can and do extend outside of their capsules but can retract in times of stress. The specimens tested here were not stained fast enough to capture a pre-retracted state and provide any insight into where and how the radiolarians extend when they do.

Though the phylogenetic tree indicates some similarity between radiolarian proteins and sponge silicateins, this could also represent similarity to cathepsin-L, a silicatein-like protein that has nothing to do with silica deposition and is instead a lysosomal enzyme. Additionally, the absence of an axial filament in phaeodarian silica rods indicates that even if silicateins are present, they are not forming silica spicules in the same way that they do in sponges.

6. CONCLUSIONS

While a perfect geodesic sphere does appear to be an applicable model to phaeodarian spheres, it is limited to integer frequencies and cannot account for irregular regions. Additionally, the way that geodesics are formed (or calculated) is by splitting a similar polyhedron and projecting onto the circumscribed sphere. This is a highly mathematical method, and a better model for sphere growth ought to have some physical or biological basis. However, further investigation into the silica deposition mechanism(s) of phaeodaria must be conducted before such a model can be created.

7. FUTURE WORK

Future work would include an elaboration upon the two additional lines of inquiry presented in the methods section: genetic analysis and staining of specimens to investigate the silica deposition mechanism. An additional stain of interest is PDMPO, which was put forth by Ogane et al. (2009) as a silica tracker in live specimens. It could potentially be used to identify growing areas of the lattice and track growth in real time.

Another area for future work is investigation into computer vision methods of constructing a 3-D digital model of a specimen. Many different computer vision software packages exist, but most are used for animation or other applications. It would be interesting and useful to apply computer vision to SEM images to stitch together a digital model of a real specimen. This would allow more detailed study of irregular areas, measurements, and analysis in the context of the whole sphere instead of being limited to one region. Such data would be invaluable in the development of a more complex model.

ACKNOWLEDGEMENTS

I would like to thank my mentor, Steve Haddock, for originating this project and for his guidance, patience, and unending programming knowledge. Thanks also to Lynne Christianson and Darrin Schultz, for teaching me so much that I cannot list it all and for having great taste in music. Thanks to Sara Tanner and Ivano Aiello for graciously allowing me to use the SEM and helping operate it. Finally, thank you to George Matsumoto, Linda Kuhnz, Z Ziccarelli, and all my fellow interns for making this summer a one-of-a-kind experience. I know that everything I've learned will help me in my future career, and I sincerely appreciate the opportunity to work with and get to know all the amazing people at MBARI.

References:

1. Coradin, T. and P.J. Lopez (2003). Biogenic silica patterning: simple chemistry or subtle biology? *ChemBioChem,* **4**: 251-259.
2. Zaremba, C.M. and G.D. Stucky (1996). Biosilicates and biomimetic silicate synthesis. *Current Opinion in Solid State & Materials Science,* **1**: 425-429.

3. Calladine, C.R. (1978). Buckminster Fuller's "tensegrity" structures and Clerk Maxwell's rules for the construction of stiff frames. *International Journal of Solids and Structures,* **14**: 161-172.
4. Thompson, D.W. 1942. On Growth and Form. New York: The Macmillan Company.
5. Anderson, O. R. 1983. Radiolaria. New York: Springer-Verlag.
6. Müller, W.E.G., X. Wang, Z. Burghard, J. Bill, A. Krasko, A. Boreiko, U. Schloβmacher, H.C. Schröder, and M. Wiens (2009). Bio-sintering processes in hexactinellid sponges: fusion of bio-silica in giant basal spicules from *Monorhaphis chuni*. *Journal of Structural Biology*, **168**: 548-561.
7. Bausch, A.R., M.J. Bowick, A. Cacciuto, A.D. Dinsmore, M.F. Hsu, D.R. Nelson, M.G. Nikolaides, A. Travesset, and D.A. Weitz (2003). Grain boundary scars and spherical crystallography. *Science*, **299**: 1716-1718.
8. Ogane, K., A. Tuji, N. Suzuki, T. Kurihana, and A. Matsuoka (2009). First application of PDMPO to examine silicification in polycystine Radiolaria. *Plankton & Benthos Research,* **4**: 89-94.

Appendix A: Side length measurements in mm

T. cygneum				*T. globosa*				*Aulosphaera*			
0.365	0.335	0.288	0.306	0.306	0.298	0.292	0.275	0.129	0.132	0.134	0.127
0.287	0.356	0.295	0.312	0.293	0.284	0.278	0.302	0.125	0.107	0.130	0.113
0.271	0.301	0.302	0.372	0.291	0.303	0.297	0.288	0.127	0.122	0.137	0.116
0.356	0.371	0.392	0.363	0.280	0.282	0.301	0.272	0.159	0.152	0.128	0.116
0.378	0.378	0.373	0.357	0.279	0.298	0.302	0.305	0.137	0.146	0.140	0.093
0.355	0.400	0.323	0.367	0.271	0.277	0.285	0.290	0.129	0.116	0.099	0.120
0.362	0.364	0.397	0.350	0.276	0.274	0.312	0.288	0.116	0.102	0.154	0.167
0.383	0.376	0.374	0.379	0.281	0.272	0.251	0.275	0.130	0.122	0.165	0.114
0.383	0.389	0.345	0.374	0.276	0.261	0.297	0.288	0.147	0.129	0.123	0.115
0.381	0.395	0.442	0.419	0.301	0.270	0.272	0.301	0.128	0.126	0.101	0.090
0.368	0.387	0.376	0.374	0.249	0.283	0.289	0.306	0.139	0.116	0.125	0.139

0.362	0.361	0.359	0.374	0.271	0.230	0.273	0.268	0.132	0.108	0.127	0.101
0.390	0.414	0.422	0.375	0.277	0.286	0.243	0.218	0.077	0.135	0.118	0.101
0.396	0.378	0.404	0.373	0.271	0.265	0.290	0.260	0.111	0.115	0.136	0.110
0.386	0.395	0.363	0.398	0.291	0.265	0.279	0.314	0.115	0.136	0.143	0.105
0.391	0.401	0.402	0.408	0.253	0.278	0.291	0.299	0.139	0.109	0.102	0.152
0.353	0.366	0.379	0.372	0.292	0.283	0.265	0.263	0.142	0.123	0.151	0.131
0.378	0.395	0.347	0.396	0.258	0.278	0.262	0.279	0.121	0.113	0.121	0.132
				0.274	0.262	0.281	0.293	0.123	0.127	0.135	0.133
				0.268	0.277	0.296	0.211	0.113	0.119	0.109	0.127
				0.298	0.239	0.279	0.230	0.107	0.121	0.149	0.150
				0.291	0.270	0.298	0.246	0.139	0.151	0.136	0.139
				0.291	0.263	0.236	0.284	0.138	0.139	0.118	0.127
				0.283	0.253	0.240	0.238	0.109	0.103	0.115	0.133
				0.205	0.217	0.262	0.220	0.125	0.127	0.140	0.161
				0.254	0.261	0.218	0.282	0.122	0.124	0.104	0.140
				0.229	0.294	0.253	0.236	0.149	0.129	0.104	0.115
				0.257	0.218	0.251	0.230	0.122	0.124	0.110	0.116
				0.218	0.254	0.258	0.217	0.142	0.113	0.092	0.136
				0.280	0.226	0.260	0.292	0.124	0.106	0.097	0.089
				0.231				0.102	0.132	0.129	0.132
								0.143	0.137	0.122	